



# CHORUS

This is the accepted manuscript made available via CHORUS. The article has been published as:

## Evidence for survival of the $\alpha$ cluster structure in light nuclei through the fusion process

J. Vadas, T. K. Steinbach, J. Schmidt, Varinderjit Singh, C. Haycraft, S. Hudan, R. T. deSouza, L. T. Baby, S. A. Kuvin, and I. Wiedenhöver

Phys. Rev. C **92**, 064610 — Published 23 December 2015

DOI: [10.1103/PhysRevC.92.064610](https://doi.org/10.1103/PhysRevC.92.064610)

# Does the $\alpha$ cluster structure in light nuclei persist through the fusion process?

J. Vadas, T. K. Steinbach, J. Schmidt, Varinderjit Singh, C. Haycraft, S. Hudan, and R. T. deSouza\*  
*Department of Chemistry and Center for Exploration of Energy and Matter, Indiana University  
2401 Milo B. Sampson Lane, Bloomington, Indiana 47408, USA*

L. T. Baby, S. A. Kuvin, and I. Wiedenhöver  
*Department of Physics, Florida State University, Tallahassee, Florida 32306, USA*

**Background:** Despite the importance of light-ion fusion in nucleosynthesis, a limited amount of data exists regarding the de-excitation following fusion for such systems.

**Purpose:** To explore the characteristics of  $\alpha$  emission associated with the decay of light fused systems at low excitation energy.

**Method:** Alpha particles were detected in coincidence with evaporation residues (ER) formed by the fusion of  $^{18}\text{O}$  and  $^{12}\text{C}$  nuclei. Both  $\alpha$  particles and ERs were identified on the basis of their energy and time-of-flight. ERs were characterized by their energy spectra and angular distributions while the  $\alpha$  particles were characterized by their energy spectra, angular distributions, and cross-sections.

**Results:** While the energy spectra and angular distributions for the  $\alpha$  particles are relatively well reproduced by the statistical model codes, EVAPOR and PACE4, the measured cross-section is substantially underpredicted by the models. Examination of the relative  $\alpha$  emission probability for similar systems reveals that this underprediction is a more general feature of such light-ion reactions.

**Conclusion:** Comparison of the measured relative  $\alpha$  cross-section at low  $E_{\text{c.m.}}$  for  $^{18}\text{O} + ^{12}\text{C}$ ,  $^{16}\text{O} + ^{12}\text{C}$ , and  $^{16}\text{O} + ^{13}\text{C}$  indicates that the  $\alpha$  cluster structure of the initial projectile and target nuclei influences the  $\alpha$  emission following fusion. The underprediction of the relative  $\alpha$  emission by the statistical model codes emphasizes that the failure of these models to account for  $\alpha$  cluster structure is significant.

PACS numbers: 21.60.Jz, 26.60.Gj, 25.60.Pj, 25.70.Jj

## I. INTRODUCTION

Nuclear fusion is a phenomenon of considerable significance from both the fundamental and societal perspective. Synthesis of the elements in both stellar [1, 2] and non-stellar [3–5] environments is principally governed by nuclear fusion. Attempts to synthesize superheavy elements at the limits of stability rely on fusion reactions [3]. Not only do fusion reactions provide the path by which both existing and potentially new elements are synthesized, but they also provide access to an enormous release of energy. In addition to powering stellar cores, it has recently been proposed that nuclear fusion reactions in the outer crust of an accreting neutron star fuel the tremendous energy release observed in X-ray superbursters [6–9]. With an energy release of  $10^{42}$  ergs, an X-ray superburst releases in just a few hours the energy output of our sun over approximately a decade. Beyond their occurrence in nature, fusion reactions are also of practical importance. Fusion weapons represent the largest terrestrial energy release achieved by human beings to date. Moreover, the quest to harness the sustained energy release of fusion remains the focus of considerable effort [10, 11]. Due to the important role fusion reactions play, they have been intensively studied both experimentally and theoretically for several decades.

For many systems, fusion involves the amalgamation of two nuclei into a compound nucleus which no longer retains a memory of the identity or structure of the colliding nuclei. As the two nuclei fuse, both binding energy and incident kinetic energy are converted into intrinsic excitation and spin. At energies near the Coulomb barrier, the resulting compound nucleus, characterized by its spin and excitation energy, de-excites by emitting neutrons, protons,  $\alpha$  particles, and  $\gamma$  rays. To describe this de-excitation of the compound nucleus a statistical framework is typically invoked [12, 13]. The defining features of the de-excitation process are the energy spectra and angular distributions of the emitted particles along with their cross-sections. Although this perspective of fusion reactions, namely the complete equilibration of the projectile and target nuclei followed by their statistical decay has been largely successful, exceptions have been noted [14]. In these cases, it has been noted that entrance channel effects are observable. To test this survival of entrance channel effects in fusion reactions, we investigate the collision of light nuclei with well established  $\alpha$  cluster structure [15, 16]. The extent to which this pre-existing cluster structure survives the fusion process can be probed by examining  $\alpha$  particle emission as a function of incident energy. In this paper we examine  $\alpha$  emission in the reaction  $^{18}\text{O} + ^{12}\text{C}$  for  $E_{\text{c.m.}} = 6.5$  to 14 MeV.

---

\* desouza@indiana.edu

## II. EXPERIMENTAL PROCEDURE

The experiment was conducted at Florida State University where a beam of  $^{18}\text{O}$  ions was accelerated to energies between  $E_{\text{lab}} = 16.25$  MeV and 36 MeV using the FN tandem and pulsed at a frequency of 12.125 MHz. After optimizing the beam optics, the beam intensity was decreased to  $1.5\text{-}4 \times 10^5$  p/s to facilitate comparison with future experiments using low intensity radioactive beams [17].

In the experimental setup the beam first passed through an upstream microchannel plate (MCP) detector designated US MCP. In this detector, passage of the  $^{18}\text{O}$  ions through a carbon foil produces secondary emission electrons which are transported to an MCP situated out of the beam path by crossed electric and magnetic fields. Arrival of the electrons at the MCP produces a fast timing signal [17]. The beam subsequently impinged on a second MCP detector designated TGT MCP approximately 1.3 m downstream of the US MCP. The 93  $\mu\text{g}/\text{cm}^2$  thick carbon foil in the TGT MCP served both as the target for the experiment as well as a secondary emission foil for this MCP. Measurement of the time-of-flight (TOF) between the two MCPs allowed rejection of beam particles scattered or degraded prior to the target as well as provided a direct measure of the number of beam particles incident on the target. The fast timing signal of the TGT MCP was also used to measure the TOF for reaction products.

In the angular range  $4.3^\circ \leq \theta_{\text{lab}} \leq 11.2^\circ$  reaction products were detected using a segmented, annular silicon detector which provided both an energy and fast timing signal [18]. The detector used in this experiment was a new design fabricated by Micron Semiconductor designated S5. The detector which was nominally 220  $\mu\text{m}$  thick consisted of sixteen pie-shaped sectors on its ohmic surface. On its junction side, the detector was segmented into six concentric rings subdivided into four quadrants. The segmentation of this design was optimized for the kinematics associated with the study of low energy fusion reactions. Reaction products were also detected in the angular range  $12^\circ \leq \theta_{\text{lab}} \leq 23^\circ$  using another annular silicon detector (design S1), 300  $\mu\text{m}$  thick, situated closer to the target. This detector was similar to the S5 detector previously described but had sixteen concentric rings spanning the angular range which are sub-divided into quadrants. With this experimental setup the efficiency for detection of fusion residues ranged from 72% at the lowest incident energy to 67% at the highest incident energy. Further details on the operating performance of these detectors and the experimental setup are described in Refs. [17] and [19].

## III. CHARACTERISTICS OF THE EVAPORATION RESIDUES

A typical energy vs. time-of-flight (ETOF) spectrum measured is presented in Fig. 1 where the energy corresponds to the energy deposited in the silicon detector while the time-of-flight is the time difference between the target MCP and the silicon detector. The prominent feature in the spectrum is the peak associated with elastically scattered particles located at  $E_{\text{Si}} = 25$  MeV and a TOF of approximately 10 ns. Extending from this peak to lower energies is a locus of points that exhibit a characteristic energy-TOF relationship. This locus corresponds to scattered beam particles and has a total intensity of approximately 2% of the elastic intensity. Situated at longer TOF than the beam scatter is a clear island corresponding to the detection of nuclei with  $A > 18$ . Located at shorter times than the beam scatter are two distinct islands. Located between  $E_{\text{Si}} \approx 8$  MeV and 20 MeV and a TOF of 4-7 ns is a locus corresponding to the detection of  $\alpha$  particles. The expected correlation between energy and TOF is qualitatively manifested for these particles. Calculation of the ETOF associated with  $A=4$  confirms this assignment. At lower deposited energy,  $E_{\text{Si}} < 6$  MeV and a TOF of 4-5 ns an island corresponding to protons is also observed.

The region of Fig. 1 associated with  $A > 18$  is due to fusion of  $^{18}\text{O}$  nuclei with  $^{12}\text{C}$  nuclei. The resulting  $^{30}\text{Si}$  nuclei de-excite via emission of neutrons, protons, and  $\alpha$  particles producing evaporation residues. Detection of the evaporation residues provides a direct measure of the fusion cross-section [19].

Presented in Fig. 2 is the laboratory angular distribution of evaporation residues for incident energies  $E_{\text{lab}} = 16.25$  MeV to 36 MeV. Also shown are the evaporation residue angular distributions predicted by the statistical model codes EVAPOR [20] (solid red line) and PACE4 [21] (dashed blue line), which employ a Hauser-Feshbach formalism to describe the de-excitation of the fusion product. At all energies the yield for evaporation residues decreases with increasing laboratory angle. Closer examination of the angular distributions reveals that the distributions have a two component nature that can be qualitatively understood in the following context. De-excitation of the fusion product via single or few nucleon emission will impart less transverse momentum to the recoiling evaporation residue resulting in an angular distribution that is peaked at smaller angles. In contrast, emission of an  $\alpha$  particle will result in a larger transverse momentum for the evaporation residue and as a result an angular distribution that is peaked at larger angles. While the small angle component of these distributions is reasonably well described by the statistical model codes, the large angle component is significantly underpredicted.

The energy distributions of evaporation residues are shown in Fig. 3 for different incident energies. It should be noted that the distributions presented correspond to

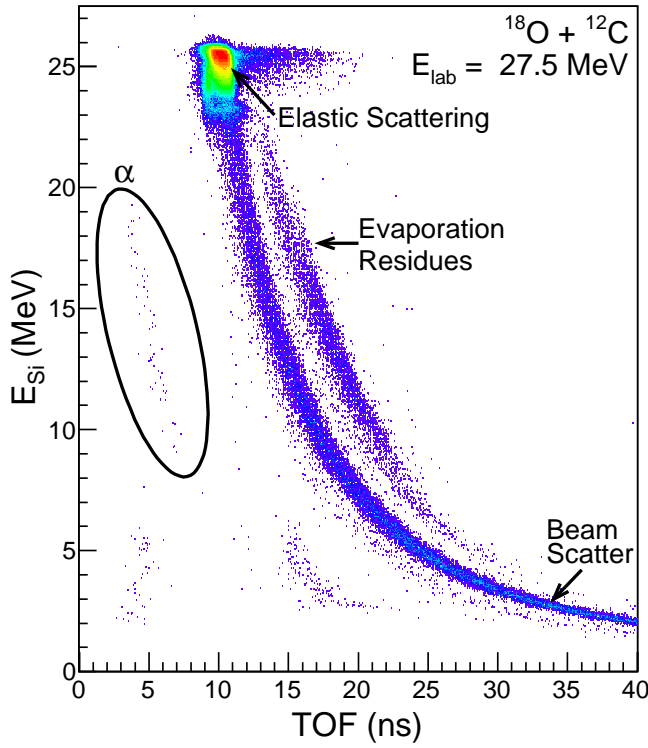


FIG. 1. (Color online) Energy versus time-of-flight spectrum of reaction products with  $4.3^\circ \leq \theta_{lab} \leq 11.55^\circ$ . Color represents yield on a logarithmic scale.

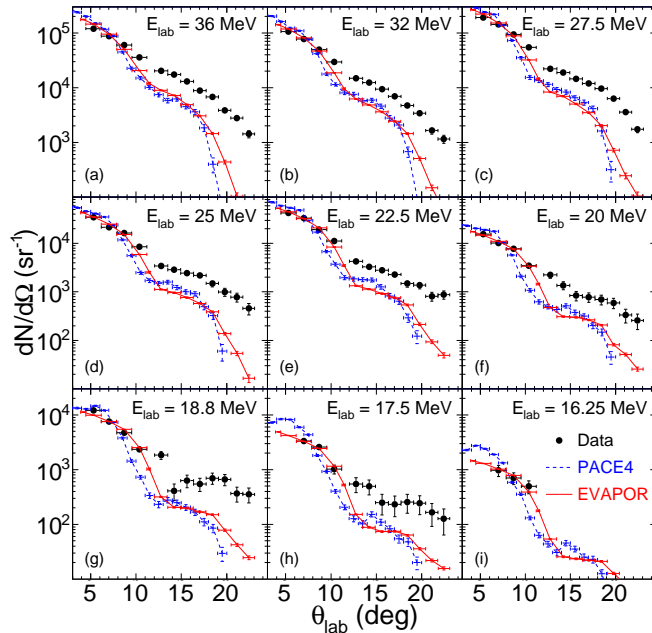


FIG. 2. (Color online) Angular distribution of evaporation residues in the laboratory frame for different bombarding energies for  $^{18}\text{O} + ^{12}\text{C}$ . Solid symbols depict the experimental angular distribution while the solid and dashed curves indicate the angular distributions predicted by the statistical model codes EVAPOR and PACE4 respectively. The model angular distributions have been normalized to the experimental data over the angular range  $4.3^\circ \leq \theta_{lab} \leq 11.2^\circ$ .

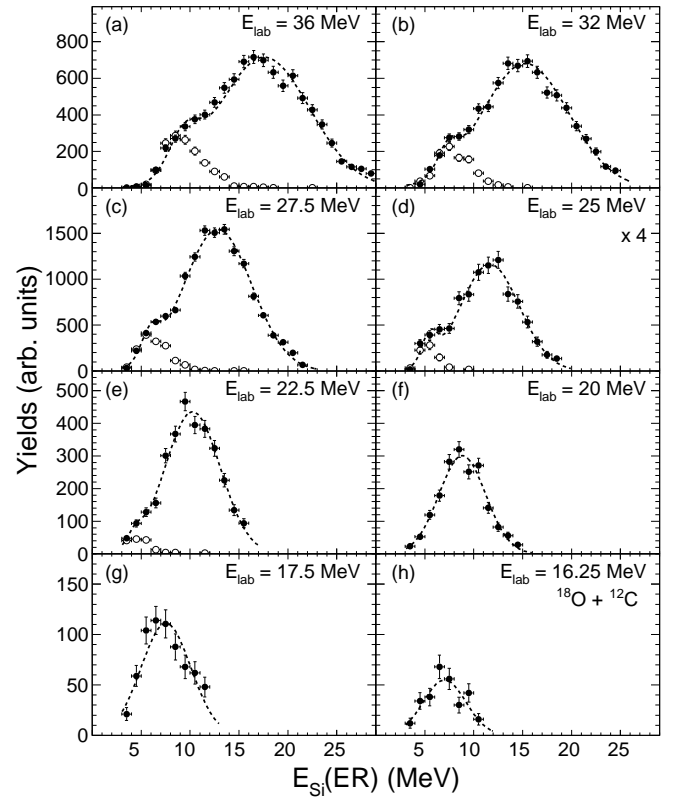


FIG. 3. Solid symbols depict the distribution of deposited energies in the Si detector for evaporation residues at different bombarding energies. Open symbols correspond to the same quantity for which evaporation residues are coincident with  $\alpha$  particles. Open symbols have been scaled by a factor of two for clarity. The dashed line corresponds to a two Gaussian fit.

the energy deposited in the silicon detector. As the atomic number of the residues is not known the energy measured in the silicon detector has not been corrected for the energy loss in the target or the entrance dead layer of the silicon detector. If one assumes, consistent with statistical model calculations, that the evaporation residues are predominantly Si and Al nuclei, then this energy loss correction is typically of the order of 1 to 1.5 MeV. At the five higher energies a clear indication of a bimodal distribution is observed. Qualitative examination of the shape of these energy distributions indicates that the total distribution is dominated by the yield of the high energy component. This observed distribution can be well described by the sum of two Gaussians as shown by the two Gaussian fit indicated by the dashed line. For  $E_{lab} \leq 20$  MeV only a single component distribution is observed corresponding to the higher energy component present at higher beam energies.

One possible origin of the two component nature of the energy distributions visible in Fig. 3 is different de-excitation pathways for the excited  $^{30}\text{Si}$  nucleus, namely  $\alpha$  emission as compared to nucleon emission. This conclusion is also consistent with the angular distributions

observed in Fig. 2. To investigate if this hypothesis is correct, we constructed the energy distribution of evaporation residues selected on the coincident detection of an  $\alpha$  particle in the angular range  $4.3^\circ \leq \theta_{\text{lab}} \leq 23^\circ$ . The results are presented as the open symbols in Fig. 3. All the residue energy distributions coincident with an  $\alpha$  particle are single peaked with maxima at  $E_{\text{Si}} = 6-9$  MeV. The fact that the  $\alpha$  gated residue energy distributions are peaked at essentially the same location as the mean value of the low energy component and have comparable widths, provides strong evidence that the low energy component in Fig. 3 is associated with  $\alpha$  emission. The reduction of the average energy of the evaporation residue is understandable since the  $\alpha$  particle is detected at forward angles hence the recoil imparted to the evaporation residue lowers its energy.

A quantitative perspective of the trends associated with the low and high energy component is examined in Fig. 4. In the upper panel of the figure one observes that for both the high energy (open triangles) and low energy (open squares) components the average laboratory energy of the residue,  $\langle E_{\text{Si}}(ER) \rangle$ , increases essentially linearly with the incident energy  $E_{\text{c.m.}}$ . As expected, the trend for the total distribution (filled circles) follows that of the high energy component since the yield of the high energy component dominates the yield of the total distribution. The trend of the  $\alpha$  gated residue energy distributions (solid red squares) unsurprisingly follows that of the low energy component, quantitatively demonstrating that the low energy residues are associated with  $\alpha$  emission. At the lowest incident energies measured, the low energy of these evaporation residues emphasizes the need for low detection thresholds. The linear trend observed for the average energies of the residues can be understood as the change of the kinematics of the reaction with increasing incident energy. To quantitatively assess this dependence we have calculated the average laboratory energy of the  $^{30}\text{Si}$  fusion product as a function of  $E_{\text{c.m.}}$  and indicate the result as the solid line in Fig. 4. To investigate the reason for the difference between the measured values for the evaporation residues (solid circles) and that calculated for the  $^{30}\text{Si}$  (solid line) we have calculated the energy a  $^{30}\text{Si}$  nucleus would possess after it passes through the target and front dead layer of the Si detector. The impact of the target and front dead layer of the Si detector on the detected energy of the  $^{30}\text{Si}$  has been calculated using the energy loss program SRIM [22] and the result is depicted as the dotted line. Also shown in Fig. 4 is the  $\langle E_{\text{Si}}(ER) \rangle$  associated with a  $^{26}\text{Mg}$  nucleus resulting from the  $\alpha$  decay of  $^{30}\text{Si}$ . The  $\alpha$  emission is assumed to be isotropic with both the  $\alpha$  particle and evaporation residue detected in the experimental setup. The overall agreement of the dashed line with the low energy component bolsters the conclusion that the low energy component is associated with emission of an  $\alpha$  particle.

In the lower panel of Fig. 4 the trends associated with the widths of the high and low energy components of

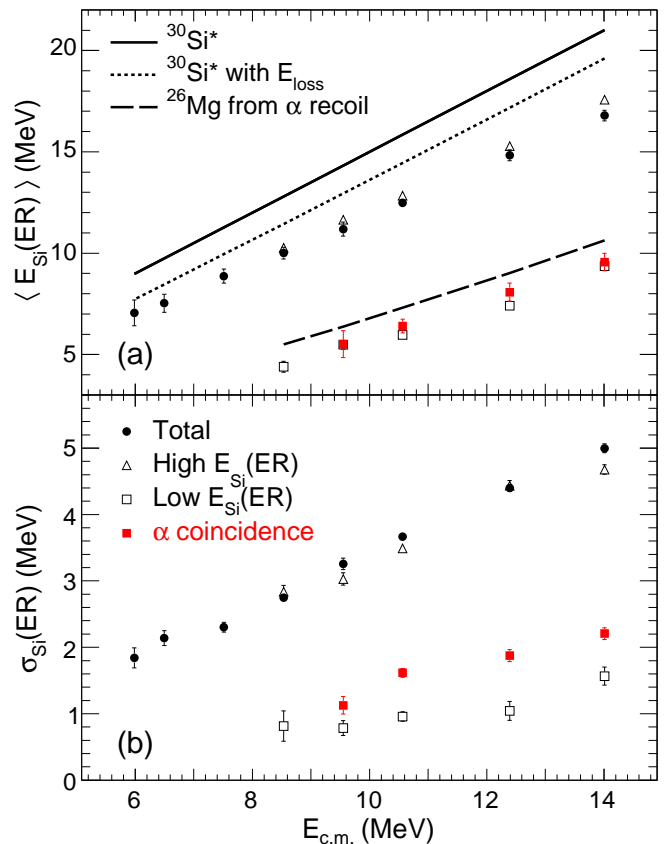


FIG. 4. (Color online) Top panel: Average energy deposited in the Si detector by fusion residues as a function of the available energy in the center-of-mass (solid circle). The mean energy extracted for the low and high energy components from the fits shown in Fig. 3 are represented by the open squares and triangles respectively, while the red closed squares correspond to residues in coincidence with  $\alpha$  particles. The solid line represents the energy of the excited compound nucleus for complete fusion. The dotted line represents the compound nucleus energy after energy loss in both the target and Si dead layer. The dashed line represents the average energy deposited by a  $^{26}\text{Mg}$  nucleus following emission of an  $\alpha$  particle. The influence of the target and Si dead layer have been accounted for in the case of the  $^{26}\text{Mg}$ . Bottom panel: Widths,  $\sigma$ , associated with the mean values shown in the top panel.

the total distributions as well as the  $\alpha$  gated distributions are shown. The widths of both components of the total distributions increase linearly with  $E_{\text{c.m.}}$  from 1.8 MeV to 5 MeV in the former case and from 0.8 to 1.6 MeV in the latter case. While the mean values of the  $\alpha$  gated distributions are in good agreement with those of the low energy component, the widths of the  $\alpha$  gated distributions are systematically slightly larger.

#### IV. ALPHA EMISSION

Having characterized the evaporation residues produced in this reaction, we next examine the measured

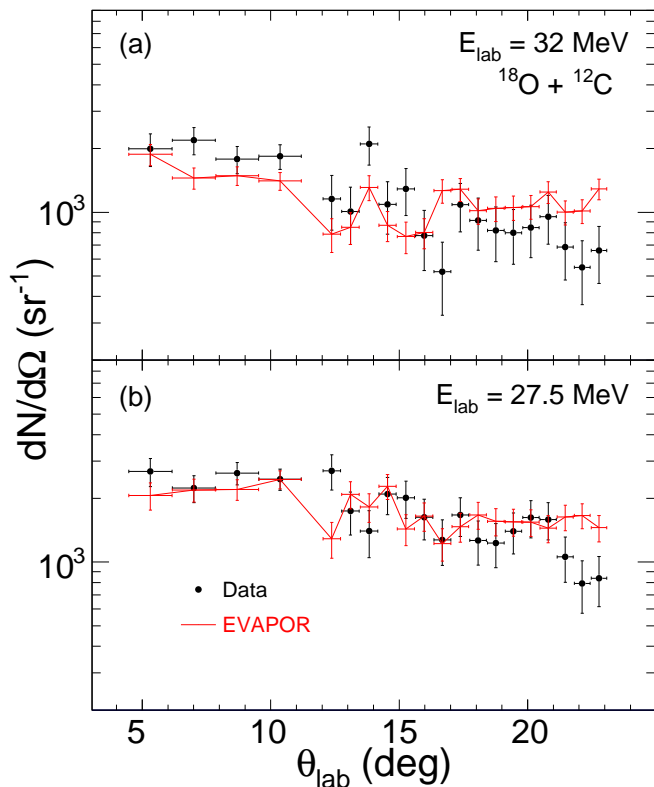


FIG. 5. (Color online) Angular distributions of  $\alpha$  particles in the laboratory frame at  $E_{\text{lab}}=32$  MeV and 27.5 MeV. The predictions of the EVAPOR model are indicated as a solid (red) line.

angular distributions of  $\alpha$  particles to ascertain if they exhibit the characteristics of statistical emission from a compound nucleus. The  $\alpha$  particles are identified based upon their position in the energy-TOF spectrum. Shown in Fig. 5 are the  $\alpha$  particle angular distributions at two incident energies along with the predictions of the EVAPOR statistical model code normalized to the data. The general trend observed is that the differential yield of  $\alpha$  particles,  $dN/d\Omega$ , decreases slightly with increasing angle. This forward peaking can be understood as being due to the center-of-mass momentum of the compound nucleus. The measured angular distributions are in relatively good agreement with the EVAPOR predictions as evident in the figure.

Having established that the  $\alpha$  angular distribution is consistent with statistical decay from the compound nucleus and plays a non-negligible role in the de-excitation of the fusion product, we directly examine the energy spectra of these emitted particles. Shown in Fig. 6 are the energy distributions of  $\alpha$  particles detected in the angular range  $4.3^\circ \leq \theta_{\text{lab}} \leq 23^\circ$ . To facilitate comparison with a statistical model, the energy of the  $\alpha$  particle has been transformed into the center-of-mass frame of the system and the resulting distributions are shown in Fig. 6 along with the EVAPOR predictions. As is evident in the figure, the statistical model provides a reasonably

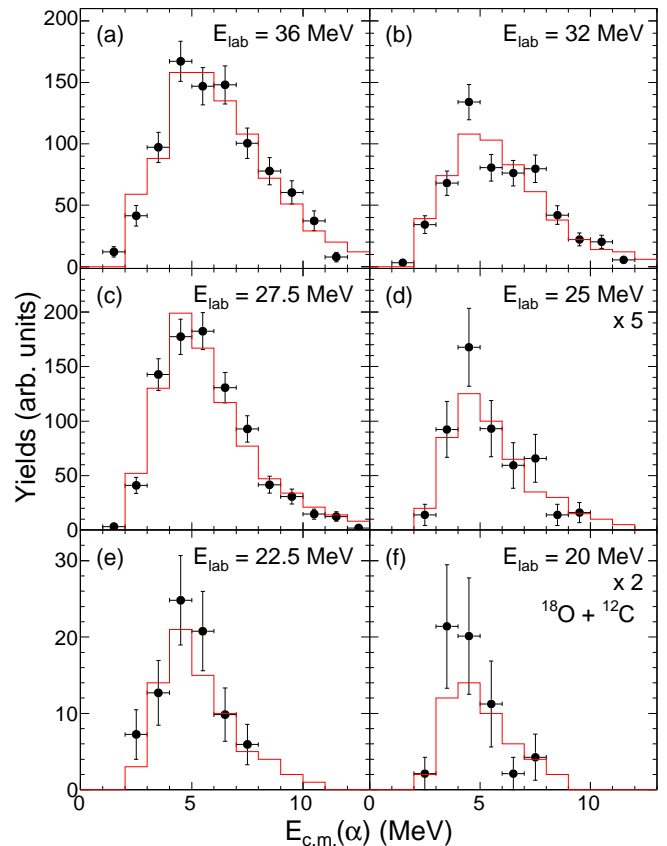


FIG. 6. (Color online) Energy of  $\alpha$  particles in the center-of-mass frame for different bombarding energies. The solid (red) line depicts the prediction of the statistical model code EVAPOR. The predictions have been normalized to the experimental ones in the energy range shown.

good description of the measured energy distributions of emitted  $\alpha$  particles.

In order to make a more quantitative analysis of the measured distributions and provide more detailed comparison with statistical model codes, we extract the first and second moments of the distributions presented in Fig. 6 and examine the dependence of these quantities on  $E_{\text{c.m.}}$  in Fig. 7. In the upper panel of Fig. 7 one observes that  $\langle E_{\text{c.m.}}(\alpha) \rangle$  increases with increasing incident energy,  $E_{\text{c.m.}}$ , both for the experimental data and the model predictions. For reference, the excitation energy,  $E^*$ , of the compound nucleus is displayed on the scale above the top panel. The error bars for the experimental data are defined by the statistics of the measurement. The results of the EVAPOR and PACE4 calculations are presented as the solid and dashed lines respectively. The overall increasing trend of the first moment,  $\langle E_{\text{c.m.}}(\alpha) \rangle$ , observed in the experimental data is reasonably reproduced by both models. EVAPOR is in better agreement with the experimental data than PACE4, which slightly overpredicts  $\langle E_{\text{c.m.}}(\alpha) \rangle$  at all energies by approximately 0.5 MeV. This deviation between PACE4 and the experimental data increases with increasing  $E_{\text{c.m.}}$ . While

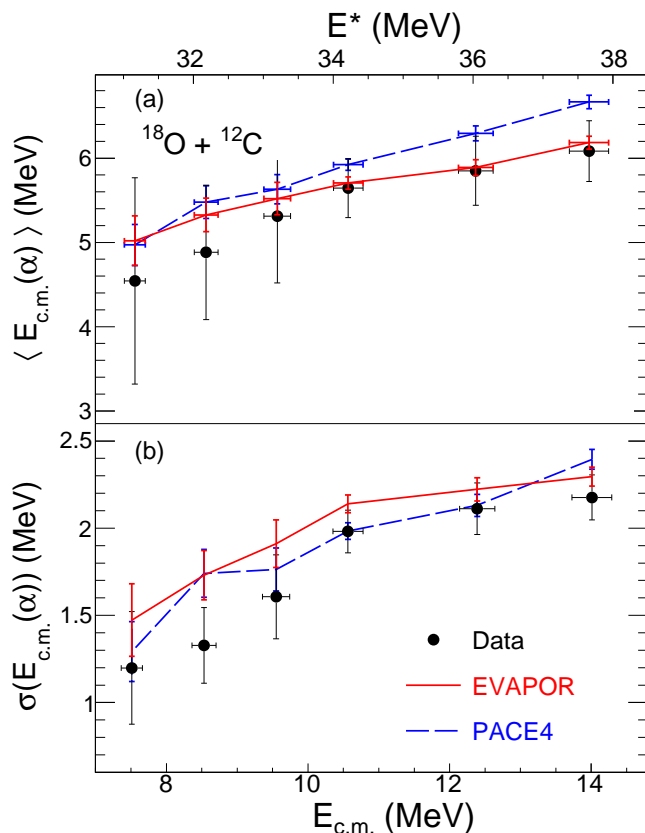


FIG. 7. (Color online) Top panel: Average energy of  $\alpha$  particles in the center-of-mass frame as a function of the available energy in the center-of-mass (solid circle). The solid (red) line represents the average energy predicted by the statistical model code, EVAPOR. The dashed (blue) line represents the average energy predicted by PACE4. Bottom panel: Widths,  $\sigma(E_{c.m.}(\alpha))$ , associated with the mean values shown in the top panel.

for the lower energies the statistical model predictions lie within the statistical uncertainties of the experimental measurement, for the two highest incident energies the statistical uncertainty is less than the deviation between the PACE4 model predictions and the measured values. Presented in the lower panel of Fig. 7 is the dependence of the second moment of the energy distributions,  $\sigma(E_{c.m.}(\alpha))$  on  $E_{c.m.}$ . The experimental widths increase from 1.2 MeV at the lowest energies to 2.2 MeV at the highest  $E_{c.m.}$ . In the case of the second moment, good agreement between the PACE4 predictions and the measured widths is observed. In contrast to the PACE4 predictions, EVAPOR predicts slightly lower values for the first moment which are in better agreement with the experimental measurement. However, in the case of the second moment EVAPOR slightly overpredicts the experimentally measured values.

In a statistical framework, two factors contribute to the  $\langle E_{c.m.}(\alpha) \rangle$  namely the temperature of the emitting nucleus and the Coulomb barrier associated with the  $\alpha$

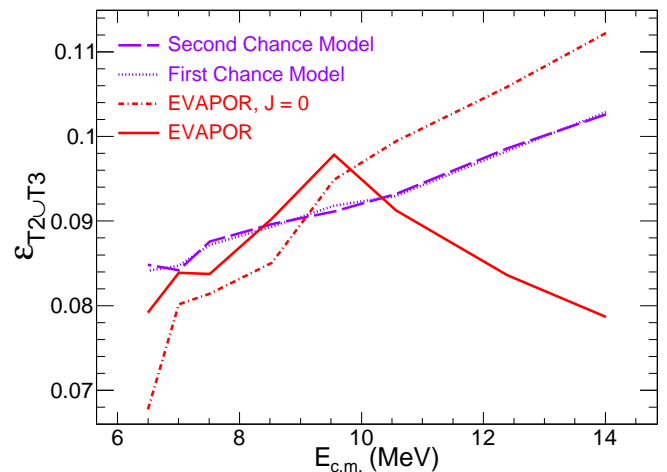


FIG. 8. (Color online) Efficiency for detection of an  $\alpha$  particle in coincidence with an evaporation residue in the experimental setup as determined by the EVAPOR model. Both the  $\alpha$  particle and evaporation residue can be detected in either the T2 or T3 silicon detectors. Also shown is the prediction of a zero spin kinematic model described in the text.

emission. As the second moment is primarily sensitive to the temperature of the emitting system, the larger disagreement of the PACE4 statistical model with the first moment suggests that the Coulomb barrier associated with  $\alpha$  emission might be slightly lower than that calculated by the model PACE4. A sensitive probe of the Coulomb barrier is the emission probability of a charged particle. We therefore examine the  $\alpha$  particle emission cross-section as a function of  $E_{c.m.}$  and compare the results to the predictions of the statistical models.

## V. EFFICIENCY CALCULATIONS

In order to extract the  $\alpha$  emission cross-section from the measured yields, it is necessary to correct for the efficiency of the experimental setup. To determine the geometric acceptance of the experimental setup the statistical model code EVAPOR was utilized. In the simplest case of isotropic single  $\alpha$  particle emission, two factors dominate the geometric efficiency, namely the center-of-mass velocity of the compound nucleus and the energy distribution of the emitted  $\alpha$  particle. Emission of additional particles, however, imparts momentum to the evaporation residue which will affect the efficiency. The efficiency determined using the EVAPOR model is shown in Fig. 8 as a solid (red) line. The efficiency for detection of an  $\alpha$  particle in coincidence with an evaporation residue ranges increases from 7.9% at  $E_{c.m.} = 6.5$  MeV to a maximum of 9.8% at  $E_{c.m.} = 9.5$  MeV. A further increase in the incident energy results in a decrease of the efficiency to  $\approx 7.8\%$  at  $E_{c.m.} = 14$  MeV. The initial increase can be understood as due to the effect of kinematic focusing.

To assess the principal factors impacting the efficiency we constructed a simple model. This model accounted for sequential two-body decays of the compound system, emitting an  $\alpha$  particle followed by a neutron (first chance) or a neutron followed by an  $\alpha$  particle (second chance). In this model, the compound nucleus,  $^{30}\text{Si}$ , travelling with a velocity,  $v_{\text{CN}}$ , along the beam direction emits the first particle. Isotropic emission is assumed consistent with zero spin. Momentum is conserved between the emitted particle and the resulting evaporation residue. The second particle is then emitted isotropically from the evaporation residue, and momentum is again conserved. The products are then subjected to a software replica of the experimental setup to determine the efficiency. The resulting efficiency is depicted as a dotted line (first chance) and a dashed line (second chance) in Fig. 8. At the lowest incident energies measured the simple model is in good agreement with the efficiency calculated using EVAPOR. For incident energies  $E_{\text{c.m.}} > 9.5$  MeV, the simple model and EVAPOR diverge. The divergence of the simple model and EVAPOR may signal the increasing importance of angular momentum which is absent in the simple model. At  $E_{\text{c.m.}} = 14$  MeV the maximum angular momentum is calculated to be  $\approx 10\hbar$ . To ascertain if the angular momentum of the compound nucleus was responsible for decrease in efficiency we calculated the efficiency for compound nuclei with zero angular momentum ( $J=0$ ) within the EVAPOR model. As can be seen in Fig. 8 for this case the efficiency increases monotonically with increasing incident energy. As the EVAPOR model includes the competition between different channels as well as the treatment of angular momentum, we utilized the efficiency determined using EVAPOR to extract the  $\alpha$  emission cross-section.

## VI. ALPHA CROSS-SECTIONS

Presented in Fig. 9 is the cross-section for  $\alpha$  decay following fusion of the  $^{18}\text{O}$  and  $^{12}\text{C}$  nuclei. In Fig. 9 one observes that the cross-section for  $\alpha$  decay increases with increasing incident energy with a shape consistent with a barrier emission process. Over the interval measured the  $\alpha$  cross-section increases from approximately 2 mb to 700 mb. The total fusion cross-section is also shown for reference. As might be qualitatively expected, at low incident energy,  $E_{\text{c.m.}}$ , only a relatively small fraction of the total fusion cross-section is associated with  $\alpha$  decay. As the incident energy increases  $\alpha$  decay becomes an increasing fraction of the total fusion cross-section. At the highest energy measured the two cross-sections are almost equal. Also shown for comparison are the predictions of the statistical model codes EVAPOR (solid line) and PACE4 (dashed line). The cross-section predicted by the models has been obtained by utilizing the relative probability for all  $\alpha$  channels and the experimentally measured total fusion cross-section. While the models exhibit the same qualitative behavior as observed

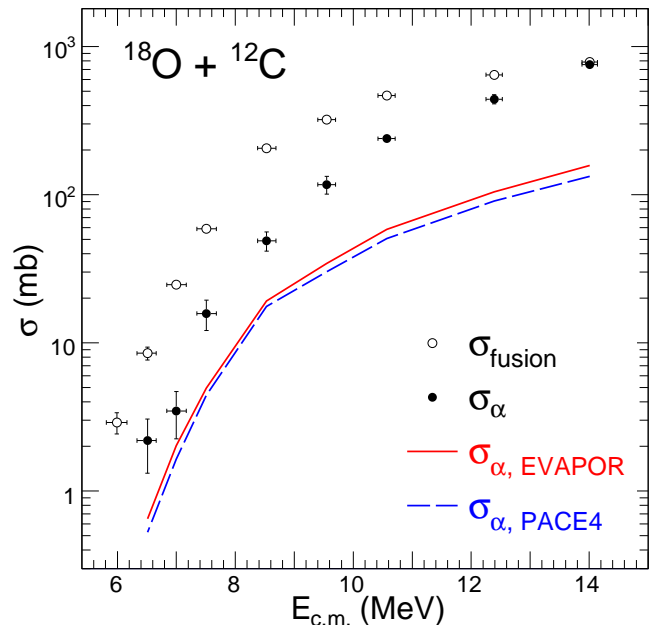


FIG. 9. (Color online) Comparison of the measured  $\alpha$  emission cross-sections (closed symbols) with the statistical model codes EVAPOR (solid red line) and PACE4 (dashed blue line). The total fusion cross-sections are shown as the open symbols.

experimentally, both EVAPOR and PACE4 substantially underpredict the experimentally measured cross-sections.

The dramatic increase in the relative cross-section for  $\alpha$  emission with excitation energy and the underprediction of the statistical model codes is emphasized in the top panel of Fig. 10. For the lowest values of  $E_{\text{c.m.}}$ ,  $\alpha$  emission comprises approximately 25% of the fusion cross-section. This fraction increases rapidly becoming essentially unity by  $E_{\text{c.m.}} \approx 14$  MeV. Over the same energy interval EVAPOR only predicts an increase in the relative  $\alpha$  emission from  $\approx 10\%$  to  $20\%$ , as shown by the solid line. From Fig. 9 it is clear that the result for PACE4 would be essentially the same. The discrepancy between the experimental data and the statistical model predictions is twofold. Not only do the statistical model calculations underpredict the magnitude of the relative  $\alpha$  particle emission, but they underpredict the rate at which  $\alpha$  particle emission increases with  $E_{\text{c.m.}}$ .

While the dramatic increase in the relative  $\alpha$  emission cross-section with incident energy and the underprediction of the statistical model codes, evident in Fig. 10, is remarkable, it should be noted that a hint of this result was already evident in the angular distribution of evaporation residues presented in Fig. 2. As observation of residues at large laboratory angles is directly related to the emission of an  $\alpha$  particle, the failure of the statistical model codes to reproduce the yield of evaporation residues at large angles suggests the underprediction of  $\alpha$  emission. Although the energies of the emitted  $\alpha$  particles are reasonably reproduced by the statistical model

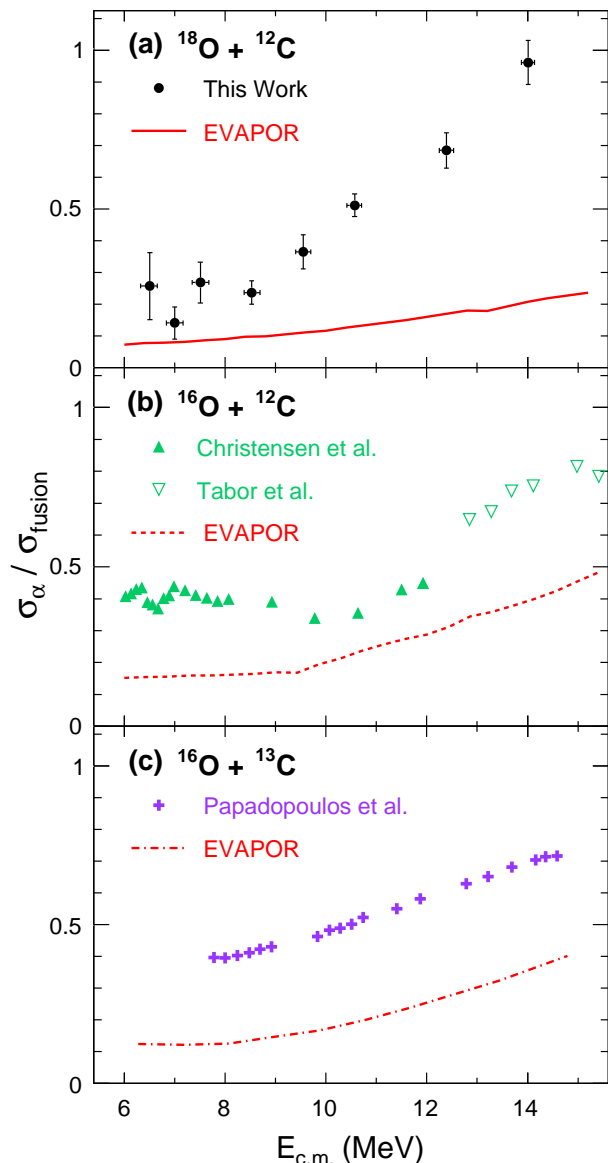


FIG. 10. (Color online) Dependence of the relative  $\alpha$  emission cross-section on  $E_{c.m.}$  for several O + C systems (Literature data are taken from Christensen [23], Tabor [24], and Papadopoulos [25]).

codes and in particular EVAPOR, the models underpredict the measured  $\alpha$  cross-section. Moreover, the magnitude of the underprediction increases with increasing incident energy. At the highest incident energy measured the statistical model code EVAPOR underpredicts the measured  $\alpha$  cross-section by a factor of approximately five.

To examine whether this underprediction of  $\alpha$  decay by the statistical model is limited to just this reaction or is a more general feature of similar light-ion reactions we examine in the middle and lower panels of Fig. 10 the relative  $\alpha$  emission fraction for  $^{16}\text{O} + ^{12}\text{C}$  [23, 24] and  $^{16}\text{O} + ^{13}\text{C}$  [25]. Juxtaposed with the experimental data are

the corresponding predictions by the EVAPOR model. In all cases the statistical model clearly underpredicts the experimental data indicating that the underprediction of  $\alpha$  decay is a more general feature of light-ion fusion reactions.

In comparing the experimental data in Fig. 10 with the EVAPOR predictions, two features are evident. The first feature is the observation of an enhanced  $\alpha$  emission at the lowest incident energies. This feature is observed for all of the three systems examined. It should be noted that the  $\alpha$  fraction for  $^{18}\text{O} + ^{12}\text{C}$  at low  $E_{c.m.}$  is approximately 25%, significantly less than the 40% observed for the  $^{16}\text{O} + ^{12,13}\text{C}$  reactions. The second feature is the increase in the  $\alpha$  fraction with increasing incident energy. While the experimental data in  $^{18}\text{O} + ^{12}\text{C}$  manifests a stronger dependence as compared to the statistical model code, the dependence in  $^{16}\text{O} + ^{13}\text{C}$  is similar in magnitude to the model predictions. The dependence for the experimental data in  $^{16}\text{O} + ^{12}\text{C}$  appears to be slightly stronger than the model predictions. The comparison for the  $^{16}\text{O} + ^{12}\text{C}$  system is complicated by the fact that two different datasets have been utilized to span the energy range of interest.

One can gain insight into understanding these two features of the offset and slope of the relative  $\alpha$  cross-section by examining the EVAPOR predictions for the three systems shown. In all three cases at low  $E_{c.m.}$  EVAPOR predicts  $\alpha$  decay to be between 8% and 15%. Initially, this fraction does not exhibit a strong dependence on incident energy. For larger  $E_{c.m.}$ , a stronger dependence of the relative  $\alpha$  emission probability is observed.

Within this context, the underprediction of the  $\alpha$  decay for all systems shown at low  $E_{c.m.}$  is noteworthy. The  $\alpha$  cluster structure of nuclei such as  $^{12}\text{C}$  and  $^{16}\text{O}$  is well established. Even for the neutron-rich nucleus  $^{18}\text{O}$  significant experimental evidence for an  $\alpha$  cluster structure exists [15, 16]. Comparison of the measured relative  $\alpha$  cross-section at low  $E_{c.m.}$  for  $^{18}\text{O} + ^{12}\text{C}$ ,  $^{16}\text{O} + ^{12}\text{C}$ , and  $^{16}\text{O} + ^{13}\text{C}$  indicates that the  $\alpha$  cluster structure of the initial projectile and target nuclei influences the  $\alpha$  emission following fusion. The lower  $\alpha$  emission probability for the  $^{18}\text{O}$  induced reaction as compared to the  $^{16}\text{O}$  induced reactions at low  $E_{c.m.}$  is in agreement with a weaker  $\alpha$  cluster nature for  $^{18}\text{O}$  relative to  $^{16}\text{O}$ . When these data are compared to the statistical model code, EVAPOR, one observes that the data exhibits a marked enhancement in  $\alpha$  emission as compared to the model. This enhancement is consistent with the  $\alpha$  cluster structure in the entrance channel surviving the fusion process and influencing the decay of the compound nucleus. The larger deviation for relative  $\alpha$  emission as compared to the EVAPOR calculations in the case of the  $^{18}\text{O}$  induced reaction suggests that neutron emission is overemphasized in the statistical model code as compared to  $\alpha$  emission.

## VII. CONCLUSIONS

In summary, we have measured evaporation residues and  $\alpha$  particles produced in the reaction  $^{18}\text{O} + ^{12}\text{C}$  at  $16.25 \text{ MeV} \leq E_{\text{lab}} \leq 36 \text{ MeV}$  and examined their angular distributions, energy spectra, as well as cross-sections. Evaporation residues exhibit a two-component angular distribution. The smaller angle component can be understood as associated with nucleon emission from the fused system and is reasonably well described by a statistical model code (EVAPOR). In contrast, the yield of the larger angle component which is associated with the emission of  $\alpha$  particles is significantly underpredicted by the model indicating that  $\alpha$  emission is enhanced relative to the predictions of the statistical model code. While the angular distributions and energy spectra of the emitted  $\alpha$  particles are in reasonably good agreement with the statistical model code predictions, the measured  $\alpha$  cross-section substantially exceeds the predicted cross-section. This enhancement of the cross-section increases from a factor of two at  $E_{\text{c.m.}} = 7 \text{ MeV}$  to a factor of nearly five at  $E_{\text{c.m.}} = 14 \text{ MeV}$ . This large relative  $\alpha$  cross-section is also observed for other light systems undergoing fusion. The underprediction of the relative  $\alpha$  emission by the statistical model code, particularly at low  $E_{\text{c.m.}}$ , reflects not only the failure of the model to account for the  $\alpha$  clus-

ter structure but the survival of this  $\alpha$  cluster structure through the fusion process.

As light-ion fusion reactions and  $\alpha$  cluster nuclei in particular play an important role in stellar nucleosynthesis, it is important to explore this observation further both experimentally and theoretically. On the experimental front, measuring  $\alpha$  emission for similar systems which lack a pronounced  $\alpha$  cluster structure in the projectile and target nuclei is necessary to determine if an  $\alpha$  cluster structure in the entrance channel is necessary to observe the enhancement. While acquiring high quality experimental data in a systematic fashion is crucial, a complete understanding of this phenomenon will require a theoretical model capable of treating the  $\alpha$  cluster structure in the entrance channel and its survival through the fusion process.

## VIII. ACKNOWLEDGMENTS

We wish to acknowledge the support of the staff at Florida State University's John D. Fox accelerator in providing the high quality beam that made this experiment possible. This work was supported by the U.S. Department of Energy under Grant No. DE-FG02-88ER-40404 (Indiana University) and the National Science Foundation under Grant No. PHY-1064819 (Florida State University).

- 
- [1] Y. E. Penionzhkevich, *Physics of Atomic Nuclei* **73**, 1460 (2010).
  - [2] P. F. F. Carnelli *et al.*, *Phys. Rev. Lett.* **112**, 192701 (2014).
  - [3] V. I. Zagrabaev, A. V. Karpov, and W. Greiner, *Phys. Rev. C* **85**, 014608 (2012).
  - [4] B. B. Back, H. Esbensen, C. L. Jiang, and K. E. Rehm, *Rev. Mod. Phys.* **86**, 317 (2014).
  - [5] R. Yanez *et al.*, *Phys. Rev. Lett.* **112**, 152702 (2014).
  - [6] T. Strohmayer and L. Bildsten, *Compact X-ray Stellar Sources* (Cambridge University, 2006) p. 113.
  - [7] C. J. Horowitz, H. Dussan, and D. K. Berry, *Phys. Rev. C* **77**, 045807 (2008).
  - [8] C. J. Horowitz *et al.*, *Phys. Rev. E* **79**, 026103 (2009).
  - [9] C. J. Horowitz *et al.*, *Phys. Rev. C* **79**, 065803 (2009).
  - [10] National Research Council, *Pacing the U.S. Magnetic Fusion Program* (National Academy Press, 1989).
  - [11] E. I. Moses, *J. Phys.: Conf. Ser.* **244**, 012006 (2010).
  - [12] V. Weisskopf, *Phys. Rev.* **52**, 295 (1937).
  - [13] W. Hauser and H. Feshbach, *Phys. Rev.* **87**, 366 (1952).
  - [14] Y. Nagashima *et al.*, *Phys. Rev. C* **33**, 176 (1986).
  - [15] E. D. Johnson, Ph.D. thesis, Florida State University (2008).
  - [16] W. von Oertzen *et al.*, *Eur. Phys. J. A* **43**, 17 (2010).
  - [17] T. K. Steinbach *et al.*, *Nucl. Instr. and Meth.* **A743**, 5 (2014).
  - [18] R. T. deSouza *et al.*, *Nucl. Instr. and Meth.* **A632**, 133 (2011).
  - [19] T. K. Steinbach *et al.*, *Phys. Rev. C* **90**, 041603(R) (2014).
  - [20] N. G. Nicolis and J. R. Beene, unpublished (1993).
  - [21] A. Gavron, *Phys. Rev. C* **21**, 230 (1980).
  - [22] J. F. Ziegler, M. D. Ziegler, and J. Biersack, *Nucl. Instr. Meth.* **B268**, 1818 (2010).
  - [23] P. R. Christensen, Z. E. Switkowski, and R. A. Dayras, *Nucl. Phys. A* **280**, 189 (1977).
  - [24] S. L. Tabor *et al.*, *Phys. Rev. C* **16**, 673 (1977).
  - [25] C. T. Papadopoulos *et al.*, *Phys. Rev. C* **34**, 196 (1986).